energies

MDPI

Article

Influence Analysis of Structural Parameters on the Performance of 120° Phase Belts Toroidal Winding Solid Rotor Induction Motor

Shaofeng Chen [1], Yaofei Han [2,*], Zhixun Ma [2], Guozhen Chen [3], Shuai Xu [4] and Jikai Si [4]

1 Henan Intelligent Power Transmission and Conversion Engineering Research Center, Henan University of Urban Construction, Pingdingshan 467000, China; chensf@hncj.edu.cn
2 National Maglev Transportation Engineering R&D Center, Tongji University, Shanghai 201804, China; zhixun.ma@tongji.edu.cn
3 School of Electronics and Information Engineering, Tongji University, Shanghai 201804, China; chgzh@tongji.edu.cn
4 College of Electric Engineering, Zheng Zhou University, Zheng Zhou 450001, Henan, China; xszzu2020@zzu.edu.cn (S.X.); sijikai@zzu.edu.cn (J.S.)
* Correspondence: ei_zx@tongji.edu.cn; Tel.: +86-186-1666-9858

Received: 16 August 2020; Accepted: 12 October 2020; Published: 15 October 2020

check for updates

Abstract: 120° phase belt toroidal winding solid rotor induction motor (120°PBTWSRIM) has advantages of simple structure, short end winding, and high overload capacity, thus it has good development prospects. To study the influence of different structural parameters on 120°PBTWSRIM performance, the 2D finite element model is established, and the electromagnetic characteristics are analyzed. The influence of six structure parameters on the average output torque, power factor, and torque ripple are analyzed, which are slot opening width, slot opening height, slot width, slot height, slot radius, and copper layer thickness. It is found that copper layer thickness has a significant effect on the performance of 120°PBTWSRIM. When the copper layer thickness is 0.5 mm, locked average output torque is increased to 2.784 Nm, locked power factor is increased by 64.6%, and locked torque ripple is reduced by 79.7%. Finally, a prototype of 120°PBTWSRIM is built and experimented, the correctness of performance influence analysis is verified by the comparison of results of the simulation and the experiment.

Keywords: electromagnetic characteristics; influence analysis; 120° phase belt toroidal winding; solid rotor induction motor; structural parameters

1. Introduction

With the merits of simple structure, high reliability, and good starting performance, the solid rotor induction motor (SRIM) is applied in many fields [1]. Toroidal winding structures are used in various applications due to their short end winding, low maintenance cost, and flexible speed regulation, such as high-frequency inductors, transformers, and electric machines [2–4].

In the 1920s, Russian scientists, K. I. Shenfer and J. S. Bruk [5], initiated research in the field of induction motors with solid rotors [5]. Early research focuses on the calculation of the equivalent circuit of solid rotor induction motors. In recent decades, many researchers and engineers worldwide contributed to the rotor topological structure [6–9]. At present, the topological structure of solid rotors is mainly divided into smooth solid rotors, slotted solid rotors, copper-plated solid rotors, and squirrel cage solid rotors. Compared with other types of solid rotors, the copper-plated solid rotor has been widely studied because of high strength and high output torque.

There are applications of toroidal winding structures in various types of motors [10–14]. The dynamic analysis of a toroidal winding switched reluctance motor (TSRM) is analyzed [10]. A new single, continuous, multi-wire winding type of TSRM is proposed and its developed performance is compared with conventional switched reluctance motors [11]. To improve the torque density and efficiency of the motor, a novel self-bearing motor is developed based on a toroidally-wound brushless DC motor [12]. A novel toroidally wound permanent magnet machine is presented [13]. Meanwhile, the performance of an external rotor induction motor with multipole stator winding is studied in [14].

Applying toroidal winding to SRIM results in a solid rotor induction motor with toroidal winding, namely, 120° phase belt toroidal winding solid rotor induction motor (120°PBTWSRIM), that combines the advantages of a solid rotor and toroidal winding can be obtained [15]. However, the penetration depth of the rotor is small, and the magnetic field distribution area changes all the time, which leads to low average output torque, low power factor, and high torque ripple. To optimize the structure of 120°PBTWSRIM, the influence analysis of structural parameters on the performance is essential.

The rest of this paper is organized as follows. In Section 2, the motor structure, the main structure parameters are given and the electromagnetic characteristics of 120°PBTWSRIM are analyzed. In Section 3, the influence of stator structural parameters on performance is investigated. In Section 4, the influence of rotor structural parameters on performance is investigated. Section 5 shows the manufacturing and the testing of a simple prototype of 120°PBTWSRIM is carried out to verify the finite element method results. Finally, some conclusions are drawn in Section 6.

2. Structure Introduction and Electromagnetic Characteristics Analysis

2.1. The Structure of 120°PBTWSRIM

The structure of 120°PBTWSRIM is shown in Figure 1. Some major parameters of 120°PBTWSRIM are listed in Table 1.

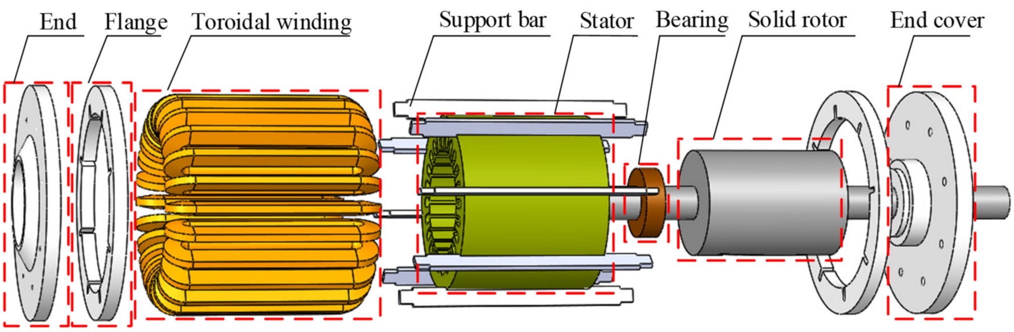

Figure 1. Configuration of 120° phase belt toroidal winding solid rotor induction motor (120°PBTWSRIM).

Table 1. 120°PBTWSRIM parameters.

Parameters	120°PBTWSRIM
Stator outer radius	130 mm
rotor outer radius	79.3 mm
Stator inner radius	80 mm
Axial length	110 mm
Air gap	0.35 mm
Pole pairs	8
Number of slots	24
Synchronous speed	375 rpm
Rated frequency	50 Hz

It can be seen that 120°PBTWSRIM is composed of stator, toroidal winding, solid rotor, end cover, bearing, flange, etc. The stator part adopts a pear-shaped slot structure. To increase the mechanical strength of the motor stator, support bars are placed on the outer surface of the stator core, which are connected to the flange and end covers. The stator and rotor are connected to the flange and end cover through a bearing. The rotor part adopts a smooth solid rotor structure. Compared with traditional laminated rotors, solid rotors are applied in many fields due to the advantages of simple structure, high reliability, and good starting performance.

It should be noted that the 120° phase belt toroidal winding structure is different from traditional toroidal winding structures. All windings of the motor are wrapped around the stator yoke in the radial direction, and the incoming end of the windings is not only located on the same side of the stator, but also have the same orientation. This structure can increase the number of pole pairs of the motor, widen the speed range of the motor, and achieve a magnetic field distribution of 24 slots and 16 poles, which is impossible to achieve in traditional windings and traditional toroidal windings. Figure 2 and Tables 2–4 show the structure diagram and magnetic field distribution of traditional winding, traditional toroidal winding, and 120° phase belt toroidal winding.

When the number of poles is small, the winding end parts are long and the toroidal winding can be a good solution. However, in the fields of bulldozers, excavators, and lifting equipment, motors are required to work under conditions that can be started frequently or locked for a long time. In these fields, the speed of the motor should not be too high, so it is necessary to increase the number of pole pairs of the motor, 120°PBTWSRIM can meet the above requirements.

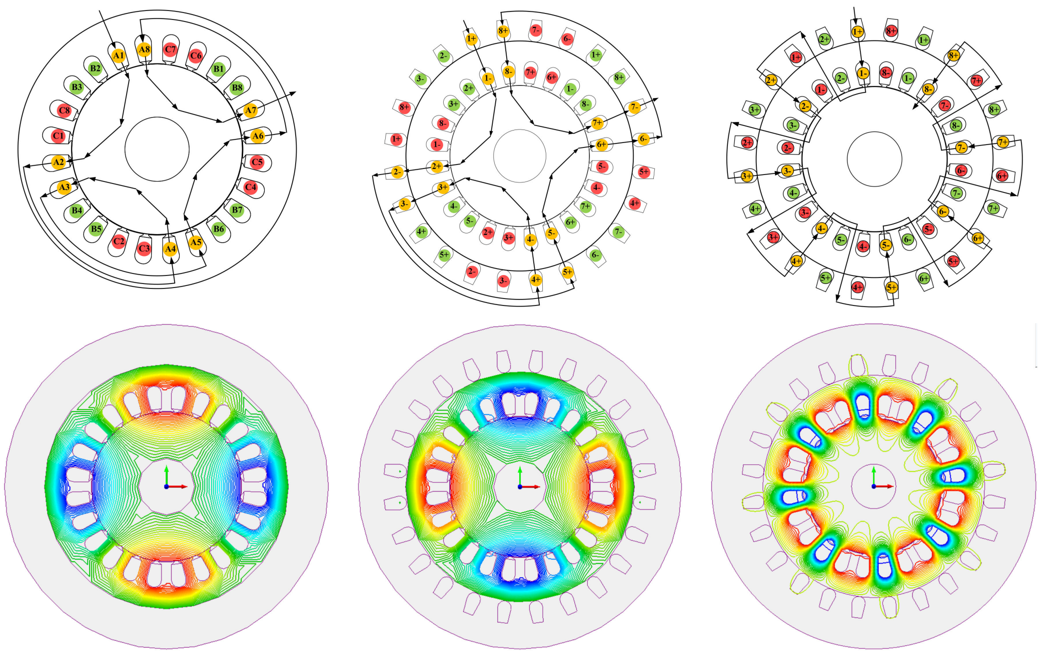

(**a**) Traditional winding (**b**)Traditional toroidal winding (**c**) 120° phase belt toroidal winding

Figure 2. The wiring and magnetic field distribution of traditional winding, traditional toroidal winding, and 120° phase belt toroidal winding.

Table 2. 12 slot winding currents for traditional winding solid rotor induction motor.

Slot No.	**1**	**2**	**3**	**4**	**5**	**6**	**7**	**8**	**9**	**10**	**11**	**12**
Phase	a	a	b	b	c	c	a	a	b	b	c	c
Current direction	+	+		●	+	+	●	●	+	+	●	●
poles			N						S			

Table 3. 12 slot winding currents for traditional toroidal winding solid rotor induction motor.

Slot No.	**1**	**2**	**3**	**4**	**5**	**6**	**7**	**8**	**9**	**10**	**11**	**12**
Phase	a	a	b	b	c	c	a	a	b	b	c	c
Out current	+	+	●	●	+	+	●	●	+	+	●	●
In current	●	●	+	+	●	●	+	+	●	●	+	+
poles			N						S			

Table 4. 12 slot winding currents for 120° phase belt toroidal winding solid rotor induction motor.

Slot No.	**1**	**2**	**3**	**4**	**5**	**6**	**7**	**8**	**9**	**10**	**11**	**12**
Phase	a	b	c	a	b	c	a	b	c	a	b	c
Out current	+	+	+	+	+	+	+	+	+	+	+	+
In current	●	●	●	●	●	●	●	●	●	●	●	●
poles	N		S		N		S		N		S	

2.2. Electromagnetic Characteristics Analysis of 120° PBTWSRIM

To study the performance of 120°PBTWSRIM, a two-dimensional finite element model was established based on the parameters in Table 1. Figure 3 shows the two-dimensional finite element model of 120°PBTWSRIM. Solver, of MagNet software, used in FEM modeling is transient 2D with motion. This paper comprehensively considers the solution time and calculation accuracy, adopts adaptive grid division, and uses different sizes of grids at different positions. The solution range is a circular area with a radius of 90 mm, and the solution time step is 1 ms. The solid rotor core material is Q235A steel, the relative magnetic permeability of steel is 400, and the conductivity of steel is 5 MS/m.

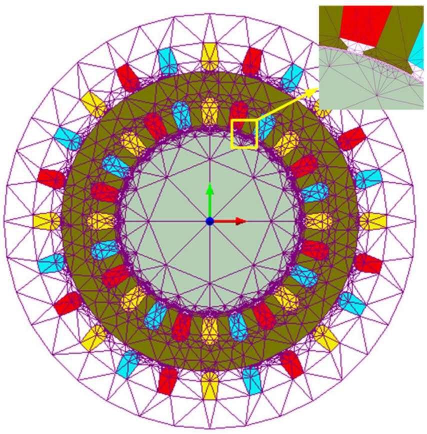

Figure 3. Two-dimensional finite element model of 120°PBTWSRIM.

Figure 3 shows the electromagnetic characteristics at different slip, such as average output torque, torque ripple, power factor, stator current, and copper loss. The formula used in the calculation process is as follows.

$$\begin{cases} T_i = \frac{P_2}{\Omega} = \frac{60\times P_2}{2\pi n}\ (i = 1, 2 \ldots N) \\ P_2 = P_1 - P_{Cu1} - P_{Fe1} - P_{mec} - P_{ad} = \sqrt{3}U_1 I_1 \cos\varphi - P_{Cu1} - P_{Fe1} - P_{mec} - P_{ad} \\ T_{ave} = \frac{T_1 + T_2 + \cdots + T_N}{N} \\ T_{ripple} = \frac{T_{max} - T_{min}}{T_{max} + T_{min}} \times 100\% \\ \cos\varphi = \frac{P_1}{S} = \frac{P_1}{\sqrt{3}U_1 I_1} \end{cases} \quad (1)$$

where, T_i $(i = 1 - N)$ is the output torque of i ms, P_2 is the output power, Ω is mechanical angular velocity, n is the speed of the motor, P_1 is the input power, P_{Cu1} is the stator copper loss, P_{Fe1} is the stator iron loss, P_{mec} is the mechanical loss, P_{ad} is the additional loss, U_1 is the line voltage, T_{ave} refers to the average output torque, S is the apparent power, T_{ripple} is the torque ripple, T_{max} is the maximum torque of steady state, and T_{min} is the minimum torque of steady state.

The current density in the motor winding is calculated as shown in Equation (2).

$$J = \frac{I_{stator}}{aN_t A_{\varnothing}} \quad (2)$$

where, I_{stator} is the rated stator phase current, a is the number of parallel branches of stator winding, N_t is the number of parallel wires, and $A_{\varnothing}$ is cross-sectional area of single wire.

Boundary conditions are usually divided into three cases [16]. The first type of boundary condition is shown in Equation (3).

$$u|_L = f_1(L) \tag{3}$$

The homogeneous second type boundary condition is shown in Equation (4).

$$\frac{\partial u}{\partial n}|_L = f_2(L) \tag{4}$$

The third type of boundary condition is shown in Equation (5).

$$\beta\frac{\partial A}{\partial n} + \alpha u = f_3(L) \tag{5}$$

In this paper, the first homogeneous boundary condition is adopted on the outer surface of the airbox, as shown in Equation (6).

$$A|_{\text{airbox}} = 0 \tag{6}$$

Figure 4 shows the electromagnetic characteristics at different slip.

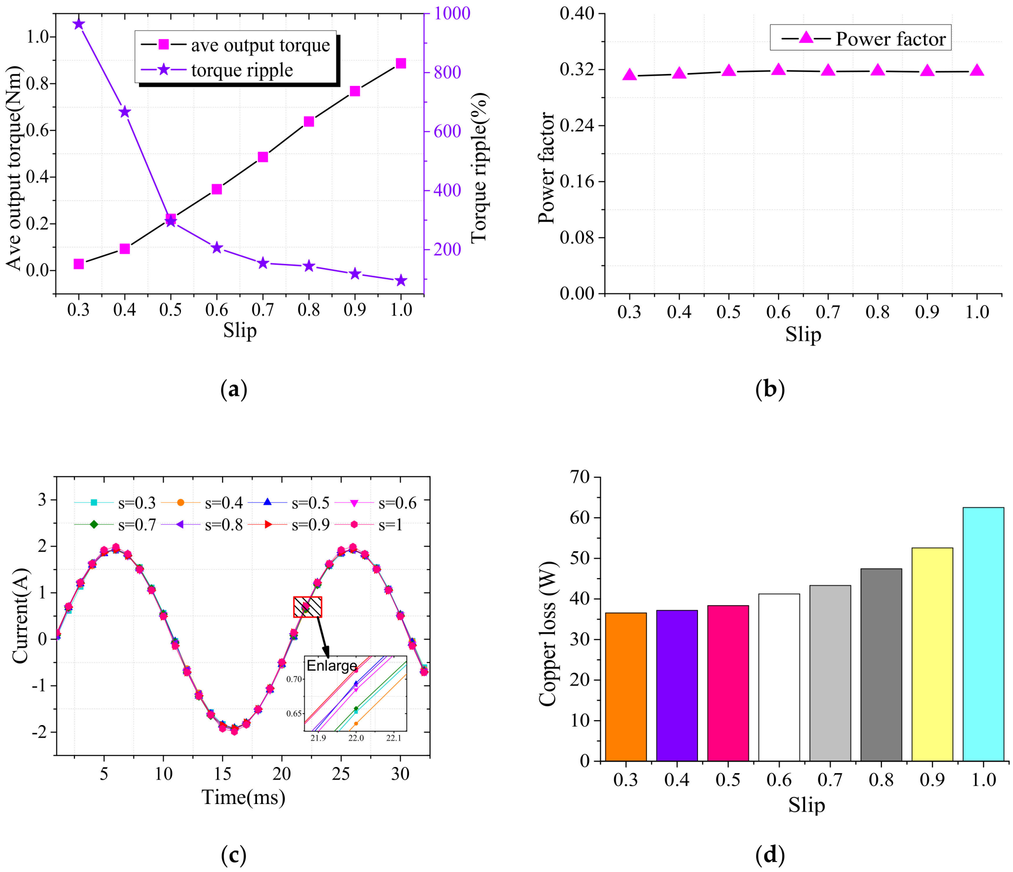

Figure 4. Electromagnetic characteristics at different slip. (**a**) Average output torque and torque ripple; (**b**) power factor; (**c**) stator current; and (**d**) copper loss.

It can be seen from Figure 4 that the average output torque and copper loss of 120°PBTWSRIM both increase with the increase of slip, the power factor and stator current only increases slightly with the increase of slip, and the torque ripple decreases with the increase of slip. The maximum average output torque of 120°PBTWSRIM is 0.887 Nm and power factor is 0.32. In general, 120°PBTWSRIM has the problems of having small output torque, low power factor, and large torque ripple, the structure parameters of the motor will affect the above performances [17]. Therefore, it is necessary to study the influence of motor structure parameters on performance.

3. Analysis Influence of Stator Structural Parameters on Performance of 120°PBTWSRIM

In order to improve 120°PBTWSRIM's shortcomings of small average output torque, low power factor, and large torque ripple, this paper studies the influence of different structural parameters on the performance of the motor from two aspects: stator structure and rotor structure. For the stator part, because slot sizes will affect the performance of the motor, the influence of different slot sizes on the performance is studied. The basic structure of the pear-shaped slot is shown in Figure 4.

It can be seen from Figure 5 that the slot structure mainly includes the slot opening width B_{S0}, the slot opening height H_{s0}, the slot width B_{s1}, the slot height H_{s12}, and slot radius R_s. The initial sizes of the stator slot are B_{S0} = 2.5 mm, H_{s0} = 0.5 mm, B_{s1} = 5.7 mm, H_{s12} = 9.5 mm, and R_s = 3.9 mm, respectively.

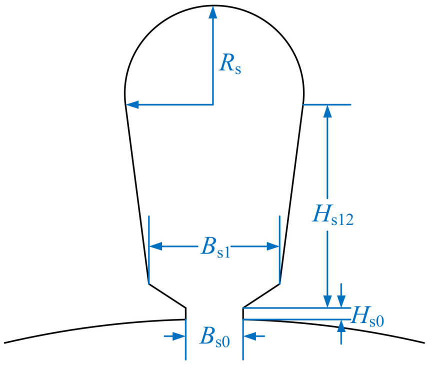

Figure 5. Size of 120°PBTWSRIM slot.

The finite element simulation software Magnet is used to simulate and analyze the influence of slot opening width, slot opening height, slot width, slot height, and slot radius on the output torque and power factor. The selection principle and range of each slot size are as follows.

(1) Slot opening width B_{S0}: due to the stator slotting, the air-gap permeability will be uneven, the magnetic permeability harmonics will be generated, and the permeability harmonic magnetic field will be generated [18]. When the slot opening width increases, the influence of harmonics on the motor will increase. Therefore, the range of slot opening width variation is 2.0–2.5 mm.

(2) Slot opening height H_{s0}: the slot opening height is smaller, the influence of its value change on the performance of motor is not easy to intuitively obtain. Considering processing difficulty and mechanical strength, the range of slot opening height variation is 0.4–0.6 mm.

(3) Slot width B_{s1}: The size of slot width will affect the size of tooth width, thereby affecting the saturation of the magnetic circuit. The range of slot width variation is 5.5–5.9 mm.

(4) Slot height H_{s12}: The size of slot height will affect yoke thickness and slot area. When the slot height increases, yoke thickness will decrease, and the saturation of the yoke will increase. When the slot height decreases, the slot area will decrease. The range of slot height variation is 8.5–10.5 mm.

(5) Slot radius R_s: Increasing slot radius will affect the area of the yoke magnetic circuit, and reducing slot radius will increase the slot full rate and the difficulty of inserting winding. The range of slot radius variation is 3.7–4.1 mm.

The range of the above slot sizes are shown in Table 5.

Table 5. The ranges of the above slot sizes are shown in Table 1.

Slot Sizes	Slot Opening Width B_{S0}	Slot Opening Height H_{s0}	Slot Width B_{s1}	Slot Height H_{s12}	Slot Radius R_s
Range (mm)	2.0–2.5	0.4–0.6	5.5–5.9	8.5–10.5	3.7–4.1

Based on the stator slot structure size parameters given above, the 120°PBTWSRIM two-dimensional finite element model is established. Under the power frequency of 50 Hz, the performance of the motor under no-load, load, and locked rotor conditions is studied, and the influence of different slot-size parameters on the average output torque and power factor is analyzed.

3.1. Slot Opening Width

To study the influence of slot opening width on the target performance in detail, and considering the mechanical strength of slot opening, the range of slot opening width is 2.0–2.5 mm. Figure 6 shows the influence of the slot opening width on average output torque and power factor under no-load, load, and locked. The slip of the motor is s = 0.7 under load steady state.

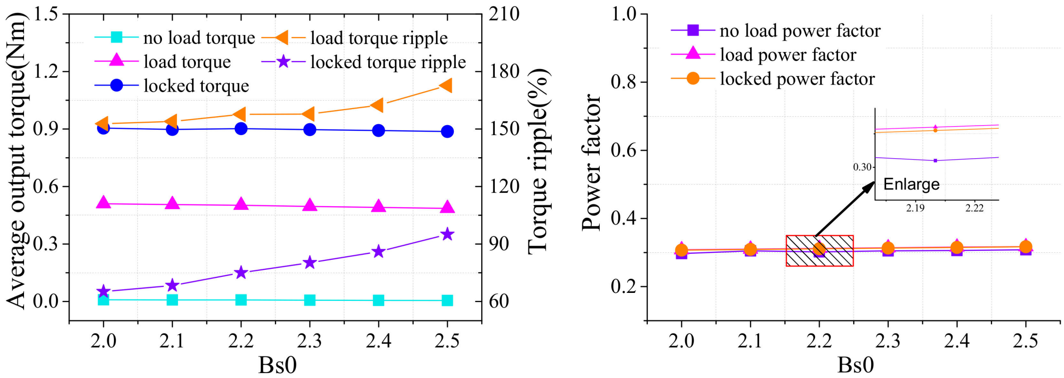

Figure 6. Influence of slot opening width on average output torque and power factor at no load, load, and locked.

Figure 6 shows that the average output torque is stable around 0 Nm under no-load, and is almost unchanged with the increase of slot opening width. The average output torque is not sensitive to the change of slot opening width. In other words, slot opening width has a small influence on the average output torque. Power factor will increase slightly with the increase of slot opening width under no-load, indicating that slot opening width has a small influence on the power factor. Torque ripple will increase with the increase of the slot opening width, but the average output torque and power factor are almost unchanged with the increase of slot opening width under load and locked. Hence, the slot opening width has a small influence on average output torque and power factor.

3.2. Slot Opening Height

Figure 7 shows the influence of slot opening height on average output torque and power factor under no-load, load, and locked. The slip of the motor is s = 0.7 under load steady state.

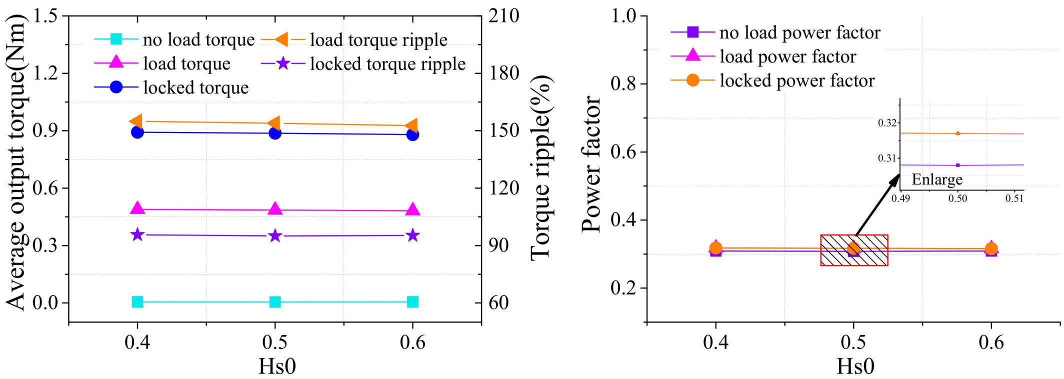

Figure 7. Influence of slot opening height on average output torque and power factor at no load, load, and locked.

As can be seen from Figure 7, the average output torque is stable around 0 Nm under no-load, and is almost unchanged with the increase of slot opening height. The average output torque is not sensitive to the change of slot opening height. In other words, slot opening height has a small influence on the average output torque. Power factor has almost not change with the increase of slot opening height under no-load, indicating that slot opening height has little influence on the power factor. The average output torque, power factor, and torque ripple almost do not increase with the increase of the slot opening height under load and locked. The average output torque and torque ripple will decrease slightly with the increase of slot opening height; the slot opening height has a small influence on average output torque and power factor.

3.3. Slot Width

Figure 8 shows the influence of slot width on average output torque and power factor under no-load, load, and locked. The slip of the motor is s = 0.7 under load steady state.

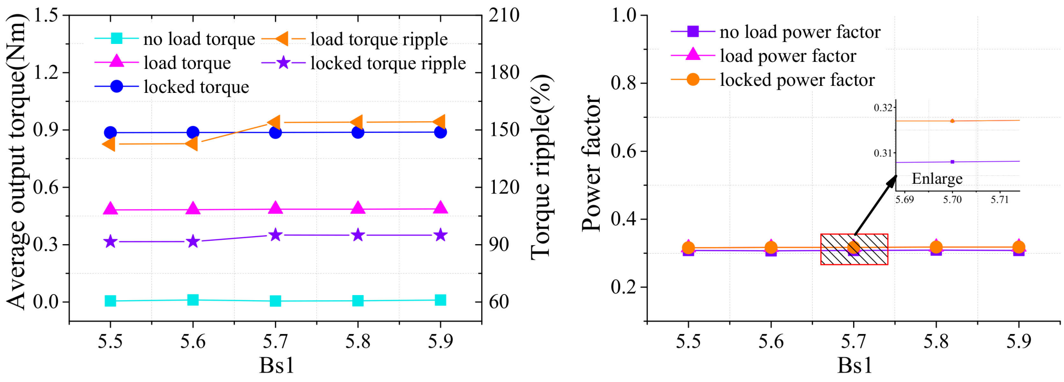

Figure 8. Influence of slot width on average output torque and power factor at no load, load, and locked.

It can be seen from Figure 8 that the average output torque and power factor are almost unchanged with the increase of slot width. The slot width has a small influence on average output torque and power factor. The average output torque and power factor are only slightly increased with the increase of the slot width under load and locked. The torque ripple will increase with the increase of the slot width, but in general, the slot width has little influence on the torque ripple.

3.4. Slot Height

Figure 9 shows the influence of slot height on average output torque and power factor under no-load, load, and locked. The slip of the motor is s = 0.7 under load steady state.

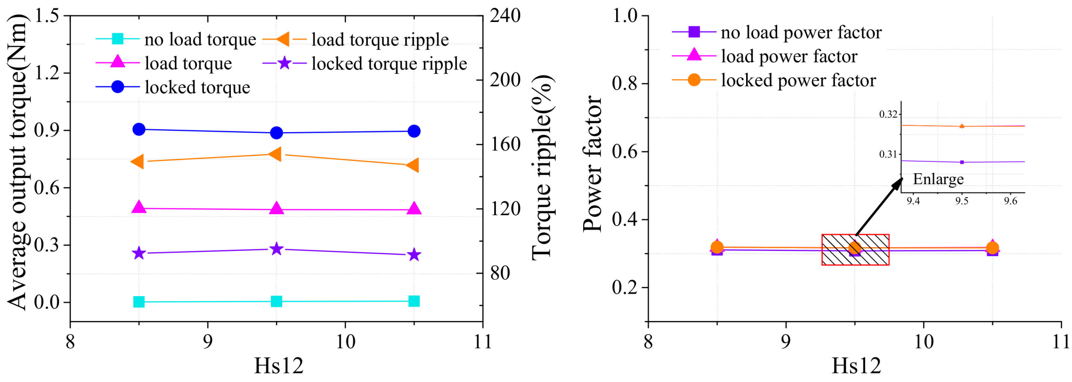

Figure 9. Influence of slot height on average output torque and power factor at no load, load, and locked.

It can be seen from Figure 9 that the average output torque and power factor are almost unchanged with the increase of slot height. The slot height has a small influence on average output torque and power factor. With the increase of slot height, the torque ripple has a maximum value, but average output torque and power factor are only slightly increased with the increase of the slot width under load and locked. The slot height has little influence on average output torque and power factor.

3.5. Slot Radius

Figure 10 shows the influence of slot radius on average output torque and power factor under no-load, load, and locked. The slip of the motor is s = 0.7 under load steady state.

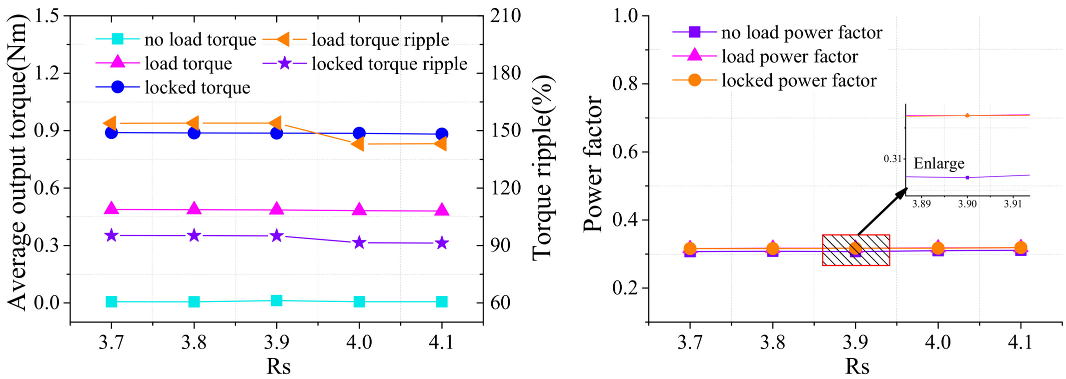

Figure 10. Influence of slot radius on average output torque and power factor at no load, load, and locked.

It can be seen from Figure 10 that the average output torque and power factor are almost unchanged with the increase of slot radius. The slot radius has a small influence on average output torque and power factor. When it is in the range 3.9–4.0 mm, the torque ripple decreases slightly, but average output torque and power factor are almost unchanged with the increase of slot radius under load and locked. The slot radius has little influence on average output torque and power factor.

According to the above analysis, it can be seen that slot opening width, slot opening height, slot width, slot height, and slot radius have little influence on average output torque and power factor. Slot opening width, slot width, slot height, and slot radius have little influence on torque ripple, and torque ripple increases with the increase of the slot opening width. However, the main optimization target such as average output torque and power factor have not changed, so the stator structure has a small influence on the output torque and power factor. The influence of rotor structure on the target performance is studied next.

4. Analysis Influence of Rotor Structural Parameters on Performance of 120°PBTWSRIM

The 120°PBTWSRIM adopts a smooth solid rotor structure, which has the disadvantages of low output torque and low power factor [1]. Copper-plated solid rotor can solve the above problems and has been widely studied. Compared with a smooth solid rotor, copper-plated solid rotor increases the depth of the magnetic field lines entering the rotor, which will significantly increase the motor output torque. Therefore, this part takes the copper-plated solid rotor as the research object to analyze the influence of different copper layer thicknesses on the motor output torque and power factor. Figure 11 shows the two-dimensional finite element model of a copper-plated solid rotor induction motor. The relative magnetic permeability of copper is 1, and the conductivity of copper is 57.7 MS/m.

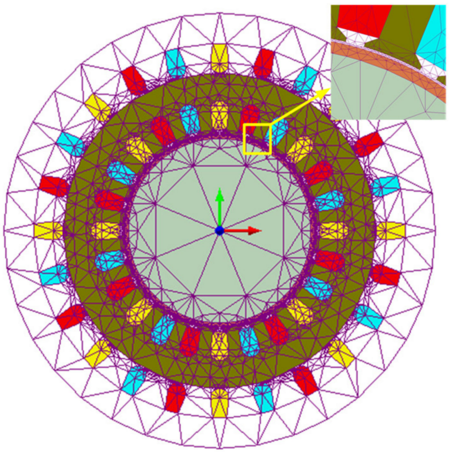

Figure 11. Finite element model of copper-plated solid rotor induction motor.

Figure 12 shows the influence of copper layer thickness on average output torque and power factor under no-load, load, and locked. The slip of the motor is s = 0.7 under load steady state.

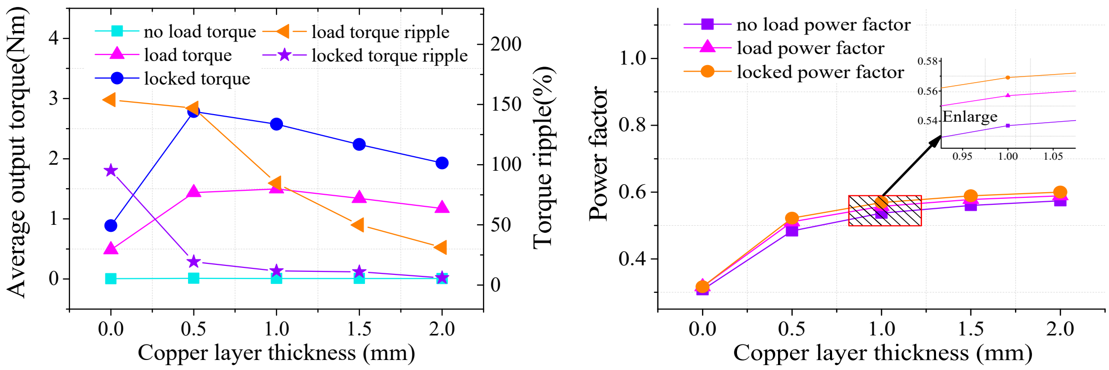

Figure 12. Influence of copper layer thickness on average output torque and power factor at no load, load, and locked.

It can be seen from Figure 12 that average output torque is stable near 0 Nm with the increase of copper layer thickness under no load, and average output torque increases rapidly until copper layer thickness gets to 1 mm and drops slowly while under load, and torque ripple decreases with the increase of the copper layer thickness under load. The average output torque increases rapidly until copper layer thickness gets to 0.5 mm and drops slowly while under locked, and torque ripple decreases with the increase of the copper layer thickness under locked. Power factor increases significantly with the increase of copper layer thickness under no load, load, and locked. In summary, copper-plated solid rotor can greatly improve the output torque and power factor of the motor. When the thickness of the copper layer is 0.5 mm, the average output torque is increased to 2.784 Nm, the power factor is increased by 64.6%, and the torque ripple is reduced by 79.7% under locked.

5. Experimental Verification

To verify the correctness of the above analysis results and 2D finite element model, a 120°PBTWSRIM prototype is processed according to the motor parameters shown in Table 1, as shown in Figure 13. The experimental platform is established, as shown in Figure 14.

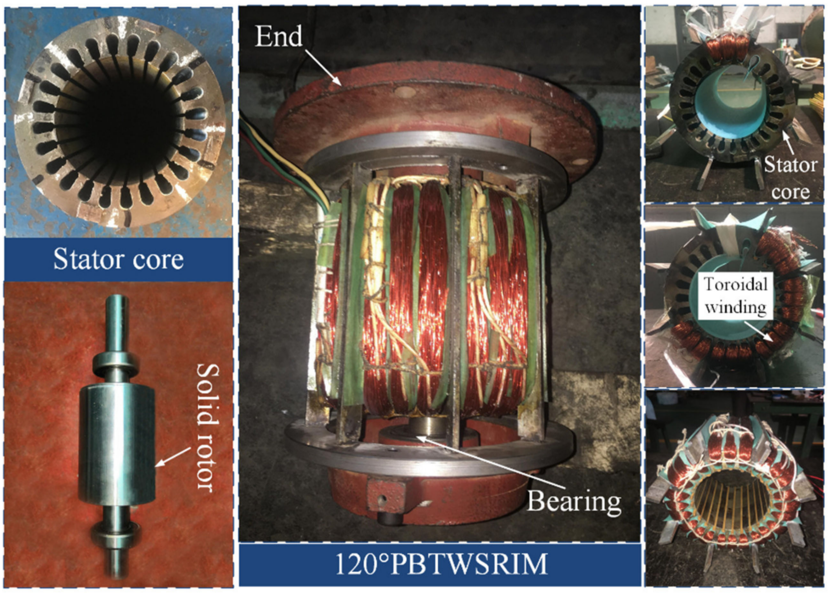

Figure 13. Prototype manufacturing process.

Figure 14. Prototype testing platform.

From Figures 13 and 14, we can see that the motor mainly consists of a stator core, toroidal winding, and solid rotor. The shell is omitted during the prototype processing, the toroidal winding is wound around the stator yoke in the radial direction, and the speed and torque of the motor are measured by the JN338 torque-speed sensor. The load torque is provided by the eddy current brake, and the experimental platform is powered by an ABB frequency converter. Under the conditions of phase voltage 380 V and frequency 50 Hz, the motor carries out no-load and load experiments. Figure 15 shows the torque-slip curve and no-load current of the finite element model and experiment. Table 6 shows the comparison results of stator currents under different slip.

It can be seen from Figure 15 and Table 6 that the torque and current under different slip of the finite element model is consistent with the torque and current under different slip in the experiment. The maximum stator current error of simulation and experiment is 6.58%, which meets the accuracy requirement. The correctness of the above analysis results and finite element model are verified.

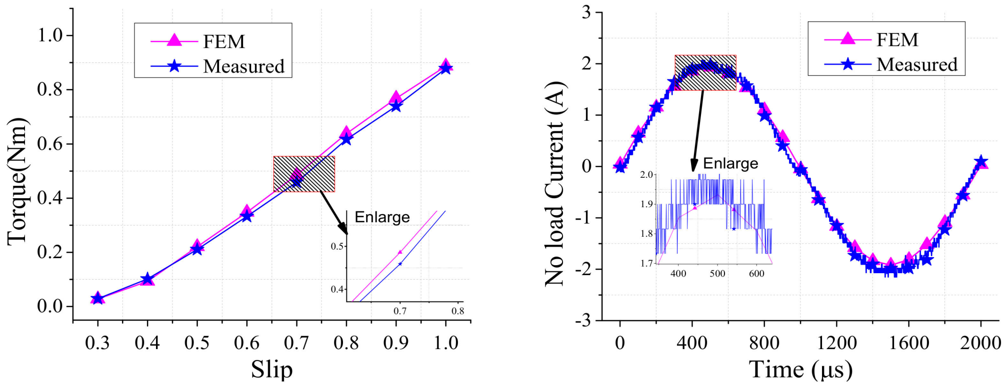

Figure 15. Torque-slip curve and no-load current of FEM and experiment.

Table 6. Stator current of FEM and experiment.

Slip	FEM	Experiment	Error
0.3	1.912 A	2.016 A	5.15%
0.4	1.913 A	2.019 A	5.25%
0.5	1.915 A	2.024 A	5.38%
0.6	1.919 A	2.032 A	5.56%
0.7	1.920 A	2.042 A	5.97%
0.8	1.923 A	2.056 A	6.46%
0.9	1.928 A	2.070 A	6.85%
1	1.951 A	2.079 A	6.15%

6. Conclusions

To study the relationship between the structure parameters and electromagnetic performance of 120°PBTWSRIM, this paper uses the finite element method to focus on the influence of structure parameters on electromagnetic performance of 120°PBTWSRIM, and the following conclusions are obtained.

(1) The slot opening width has a great influence on torque ripple, and the slot opening width will increase with the increase of torque ripple. However, the slot opening width, slot opening height, slot height, slot width, and slot radius, have almost no influence on the average output torque and power factor. When optimizing output torque and power factor, stator slot parameters should not be used as variables.

(2) The copper-plated solid rotor can effectively improve the average output torque, power factor, and torque ripple of 120°PBTWSRIM. When the copper layer thickness is 0.5 mm, the locked average output torque is increased to 2.784 Nm, the locked power factor is increased by 64.6%, and the locked torque ripple is reduced by 79.7%. The power factor increases with the increase of copper layer thickness, and the torque ripple steadily decreases with the increase of copper layer thickness. In order to increase the output torque and power factor of the solid rotor, the copper-plated solid rotor is an effective solution.

(3) The finite element results are consistent with the experimental results; the correctness of structure parameter influence analysis and finite element model is verified.

This paper focuses on analyzing the influence of structural parameters on motor performance and providing a basis for subsequent multi-objective optimization. The author has a detailed introduction to the research results of multi-objective optimization in another article.

Author Contributions: Conceptualization, S.C., Y.H., and J.S.; software, S.C., S.X., and Z.M.; validation, S.C. and G.C.; formal analysis, S.C., Y.H., and J.S.; writing—original draft preparation, S.C., G.H., S.X., and J.S.; writing—review and editing, S.C., J.S., and Y.H.; funding acquisition, S.C. and Y.H. All authors have read and agreed to the published version of the manuscript.

Funding: The research described in this paper was supported by Henan Intelligent Power Transmission and the Conversation Engineering Research Center, Henan University of Urban Construction (2020SPBH01).

Conflicts of Interest: The authors declare no conflict of interest.

References

1. Zhang, M.Y.; Tang, X.G.; Lin, J.M. Development and prospect of new type derived solid rotor asynchronous motors at home and abroad. *Electr. Eng.* **1991**, *3*, 13–15.
2. Eroglu, A. Complete modeling of toroidal inductors for high power RF applications. *IEEE Trans. Magn.* **2012**, *48*, 4526–4529. [CrossRef]
3. Hernandez, I.; de Leon, F.; Gomez, P. Design formulas for the leakage inductance of toroidal distribution transformers. *IEEE Trans. Power Deliv.* **2011**, *26*, 2197–2204. [CrossRef]
4. Feng, H.; Cui, X.; Si, J.; Gao, C.; Hu, Y. Equivalent circuit model of novel solid rotor induction motor with toroidal winding applying composite multilayer theory. *Appl. Sci.* **2019**, *9*, 3288. [CrossRef]
5. Gieras, J.F. *Handbook of Electric Motors*, 2nd ed.; Kliman, G., Tolyiat, H., Eds.; Marcel Dekker Inc.: New York, NY, USA, 2004; pp. 134–142.
6. Fu, F. Research trends of foreign solid rotor asynchronous motors. *Electr. Mach. Control Appl.* **1985**, *3*, 74–76.
7. Wang, P.; Si, J.; Feng, H.; Liu, W.; Cao, W. *Survey of Research and Development of Solid Rotor Induction Motors (Part I)*; Changzhou Fengyuan Micro and Special Motors: Chang Zhou, China, 2017; Volume 45, pp. 77–82.
8. Wang, P.; Si, J.; Feng, H.; Liu, W.; Cao, W. *Survey of Research and Development of Solid Rotor Induction Motors (Part II)*; Changzhou Fengyuan Micro and Special Motors: Chang Zhou, China, 2017; Volume 45, pp. 82–86.
9. Ho, S.L.; Niu, S.; Fu, W. A novel solid-rotor induction motor with skewed slits in radial and axial directions and its performance analysis using finite element method. *IEEE Trans. Appl. Supercond.* **2010**, *20*, 1089–1092. [CrossRef]
10. Lee, J.Y.; Lee, B.K.; Sun, T.; Hong, J.P.; Lee, W.K. Dynamic analysis of toroidal winding switched reluctance motor driven by 6-switch converter. *IEEE Trans. Magn.* **2006**, *42*, 1275–1278.
11. Marlow, R.; Schofield, N.; Emadi, A. A Continuous toroidal winding SRM with 6- or 12-Switch DC converter. *IEEE Trans. Ind. Appl.* **2016**, *52*, 189–198. [CrossRef]
12. Lee, H.; Yoo, S.; Noh, M.D. Toroidally-wound self-bearing BLDC Motor with Lorentz Force. *IEEE Trans. Magn.* **2010**, *46*, 2148–2151. [CrossRef]
13. Qu, R.H.; Lipo, T.A. Dual-rotor, radial-flux, toroidally wound, permanent-magnet machines. *IEEE Trans. Ind. Appl.* **2003**, *39*, 1665–1673.
14. Virlan, B.; Benelghali, S.; Simion, A.; Livadaru, L.; Outbib, R.; Munteanu, A. Induction motor with outer rotor and ring stator winding for multispeed applications. *IEEE Trans. Energy Convers.* **2013**, *28*, 999–1007. [CrossRef]
15. Cui, X.; Si, J.; Feng, H.; Gao, C.; Cheng, Z. Operating principle and electromagnetic characteristic analysis for large-small pole solid-rotor induction motor with toroidal windings. *Trans. China Electrotech. Soc.* **2019**, *34*, 1850–1856.
16. Tang, R. *Modern Permanent Magnet Machines Theory and Design*; China Machine Press: Beijing, China, 2019; Volume 1, pp. 62–70.
17. Si, J.; Zhao, S.; Feng, H.; Cao, R.; Hu, Y. Multi-objective optimization of surface-mounted and interior permanent magnet synchronous motor based on Taguchi method and response surface method. *Chin. J. Electr. Eng.* **2018**, *4*, 67–73.
18. Qin, H. Additional torque and torque curve calculation of small three-phase squirrel-cage asynchronous motors. *S&M Electr. Mach.* **1977**, *6*, 6–17.